Real-time imaging of accelerated solid-liquid-gas reactions with nanobubbles

Wen Wang
Southeast University
Tao Xu
Southeast University https://orcid.org/0000-0001-5436-0077
Jige Chen
Shanghai Advanced Research Institute, Chinese Academy of Sciences,
Junyi Shangguan
Lawrence Berkeley National Laboratory
Hui Dong
Xiangtan University
Huishu Ma
Shanghai Advanced Research Institute, Chinese Academy of Sciences
Qiubo Zhang
Lawrence Berkeley National Laboratory
Tingting Bai
Nanjing Medical University
Zhirui Guo
Nanjing Medical University
Haiping Fang
Shanghai Institute of Applied Physics, Chinese Academy of Sciences, Shanghai 201800
https://orcid.org/0000-0002-3496-9923
Haimei Zheng
Lawrence Berkeley National Laboratory https://orcid.org/0000-0003-3813-4170
Litao Sun (slt@seu.edu.cn)
Southeast University https://orcid.org/0000-0002-2750-5004

Research Article

Keywords: Enhanced Triple-phase Reactions, Real-time Observation, Liquid Cell Transmission Electron Microscopy, Molecular Dynamics Simulations, Etching Rate

Posted Date: November 20th, 2020

DOI: https://doi.org/10.21203/rs.3.rs-105116/v1

Version of Record: A version of this preprint was published at Nature Materials on May 26th, 2022. See the published version at https://doi.org/10.1038/s41563-022-01261-x.

Real-time imaging of accelerated solid-liquid-gas reactions with nanobubbles

Wen Wang[1,2,†], Tao Xu[1,†], Jige Chen[3,6,†], Junyi Shangguan[2,5], Hui Dong[7], Huishu Ma[6], Qiubo Zhang[2], Tingting Bai[8], Zhirui Guo[8], Haiping Fang[4]*, Haimei Zheng[2,5,]* & Litao Sun[1,*]

[1] SEU-FEI Nano-Pico Center, Key Laboratory of MEMS of Ministry of Education, Collaborative Innovation Center for Micro/Nano Fabrication, Device and System, Southeast University, Nanjing, 210096, China.

[2] Materials Sciences Division, Lawrence Berkeley National Laboratory, Berkeley, CA 94720, USA.

[3] Shanghai Synchrotron Radiation Facility, Zhangjiang Laboratory, Shanghai Advanced Research Institute, Chinese Academy of Sciences, Shanghai, 201204, China.

[4] Department of Physics, East China University of Science and Technology, Shanghai 200237, China.

[5] Department of Materials Science and Engineering, University of California, Berkeley, California 94720, USA.

[6] Shanghai Institute of Applied Physics, Chinese Academy of Sciences, Shanghai 201800, China.

[7] Key Laboratory of Welding Robot and Application Technology of Hunan Province, Engineering Research Center of Complex Tracks Processing Technology and Equipment of Ministry of Education, Xiangtan University, Xiangtan 411105, China.

[8] The Second Affiliated Hospital, Key Laboratory for Aging & Disease, Nanjing Medical University, Nanjing 210011, P. R. China.

*Correspondence to: slt@seu.edu.cn (L.S.); hmzheng@lbl.gov (H.Z.) and fanghaiping@sinap.ac.cn (H.F.).

†Contributed equally to this work

Abstract: Solid-liquid-gas reactions are ubiquitous. An understanding of how gases influence the reactions at the nanoscale is significant for achieving the enhanced triple-phase reactions. Here, we report a real-time observation of the accelerated etching of gold nanorods with oxygen nanobubbles in aqueous hydrobromic acid using liquid cell transmission electron microscopy (TEM). Our observation reveals that when an oxygen nanobubble is close to a nanorod below the critical distance (~1nm), the local etching rate is significantly enhanced with over an order of magnitude faster. Molecular dynamics simulations results show that the strong attractive van der Waals interaction between the gold nanorod and oxygen molecules facilitates the transport of oxygen through the thin liquid layer to the gold surface and thus plays a crucial role in increasing the etching rate. This result sheds light on the rational design of solid-liquid-gas reactions for enhanced activities.

Solid-liquid-gas reactions can be found in hydrogen-oxygen fuel cell reactions, heterogeneous catalysis, metal corrosion in ambient environment, and a variety of other chemical reactions (*1-7*). At the solid-liquid-gas triple-phase interfaces complex reactions occur, in which many factors may play a role including gas solubility and diffusion in liquids (*8, 9*), ion or electron transfer across the interfaces (*10*), and so on (*3, 4*). Understanding and further controlling the local environment at the triple-phase interfaces are vital to controlling the solid-liquid-gas reactions (*1,*

4, 11-13). The gaseous reactants are often dissolved in the liquid phase and then diffuse to the solid-liquid interfaces to participate in the reaction(*4, 8*). Thus, the gas solubility and transport in the liquid are generally considered to be the key factors determining the reaction rate (*4, 14-16*). Accelerated solid-liquid-gas reaction is expected as the gas solubility and diffusion in the liquid phase is increased, for instance, by increasing the solid surface area to enhance the gas absorption at the interfaces (*13, 17*), or by adding ionic liquids with higher gas solubility to form gas-diffusion layer (*1, 9, 12*). Recent studies have also shown that by delivering gases to the solid surface directly, the reaction rate was significant increased (*8, 18*). Due to the challenge of tracking the evolution of individual particles in a combined liquid and gas medium at nanoscale, the mechanisms of enhanced triple-phase reactions are still unclear.

Herein, we study the mechanisms of accelerated solid-liquid-gas reactions by taking advantages of the recent advances in in-situ transmission electron microscopy (TEM) (*19-22*). The development of liquid cell TEM (*23-29*), which allows the direct imaging of dynamic reactions in liquids, opens the opportunity to visualize the critical pathways of triple-phase reactions at the nanoscale. We investigate the etching of gold (Au) nanorods in an aqueous solution in the presence of oxygen (O_2) gases, as a model system of solid-liquid-gas reactions.

Au, as a noble metal, is often considered to be inert. However, Au nanoparticles react with the oxidative species, such as O_2 dissolved in an aqueous solution. For instance, single crystal Au nanorods can be etched completely in just a few minutes, when bubbling air into the HBr solution with Au nanorods at 70 ºC (Methods and Supplementary Figs. 1, 2). Since Au nanostructures are widely used in catalysis and sensing in biomedical applications (*30-32*), it has been of great interest to study the stability of Au nanocrystals. In this case, Au nanocrystals react with the O_2 in the solution can be described as follows:

$$AuBr_2^- + e^- \rightarrow Au \quad E = 0.959\ V \tag{1}$$

$$O_2 + 4H^+ + 4e^- \rightarrow 2H_2O \quad E = 1.299\ V \tag{2}$$

Bubbling O_2 gases in the solution significantly enhances etching of the Au nanorods, as compared to the case with the solution open to still air (as shown in Supplementary Fig. 2).

We prepare the samples for in-situ study of Au nanorod etching in HBr aqueous solution in the presence of O_2 gas using liquid cell TEM. First, the reaction solution is obtained by mixing (2:1 vol/vol) Au nanorod aqueous solution with HBr solution (1 mM). A droplet of the reaction solution (about 2 μL) is loaded onto an ultra-thin carbon film supported on a Cu frame (a TEM grid) and covered with another grid. The liquid pockets are well encapsulated between two carbon films supported on Cu frames due to van der Waals forces after the evaporation of excessive liquid solution (Methods and Fig. 1a). Thus, a simple liquid cell is achieved with liquid pockets between two ultra-thin carbon films. Then, the liquid cell is loaded into an aberration-corrected transmission electron microscope for imaging. Under the electron microscope, radiolysis of water by electron beam generates gas bubbles. Both H_2 and O_2 can be created (*33, 34*). The initial gas product is expected to be dominated by H_2; O_2 is produced at a later stage and it is much less (*35*) (also see Methods). Electron energy loss spectroscopy (EELS) of the solution with gas nanobubbles confirms the presence of O_2 gas molecules inside the nanobubbles (see the characteristics of O K-edge in Fig. 1b and Supplementary Fig. 3). Since H_2 is a reducing gas and doesn't contribute to the etching of Au (*36*), the O_2 nanobubbles can be distinguished by the enhanced etching of Au nanorods during the in-situ imaging.

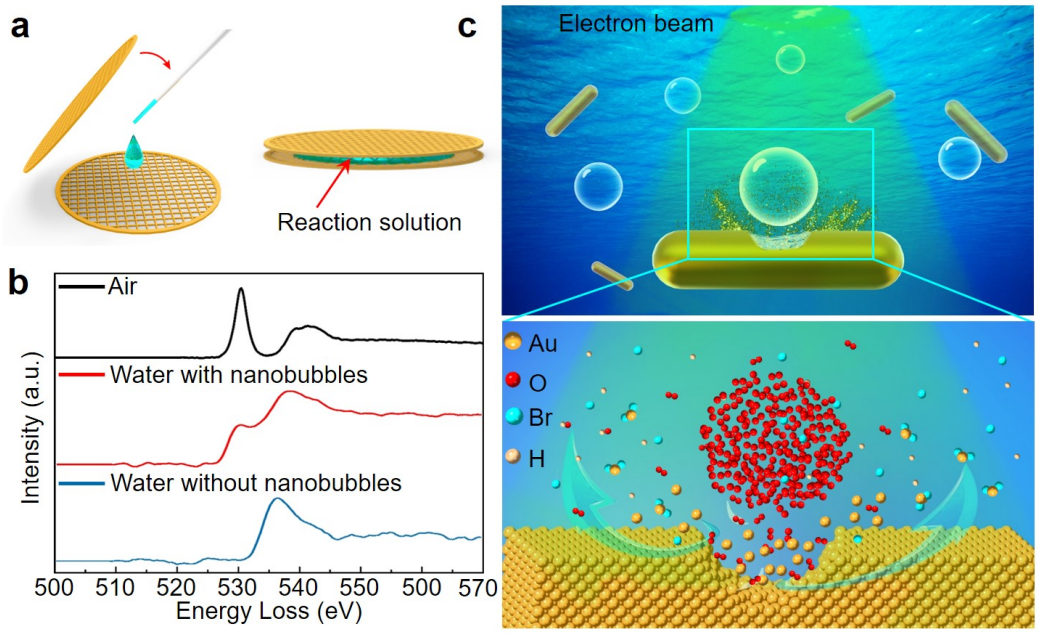

Fig. 1. Schematic illumination of a solid-liquid-gas reaction established in a liquid cell. a, Schematic liquid cell encapsulating a reaction solution. **b**, Electron energy loss spectroscopy (EELS) show O K-edge of air (black, reference spectrum from Gatan EELS Atlas), water without nanobubble (blue) and the water with nanobubbles generated by electrolysis of water at a later stage (red). The O K-edge of water with nanobubbles shows evidence of molecular O_2 at ~527 eV as compared with the reference spectrum from O_2 gas (black). **c**, Schematic illustration of the etching of gold nanorods in HBr solution with O_2 nanobubbles in the near distance.

It is noted that besides O_2 nanobubbles, other oxidative species, such as H_2O_2, $OH^{\bullet}$, and $HO_2^{\bullet}$, can also be generated during the electrolysis of H_2O. These oxidative species may also react with the Au nanorods (Supplementary Fig. 4 and Supplementary Video 1). Here, we focus on the impact of O_2 nanobubbles on the solid-liquid-gas reaction of Au nanorods (Fig. 1c).

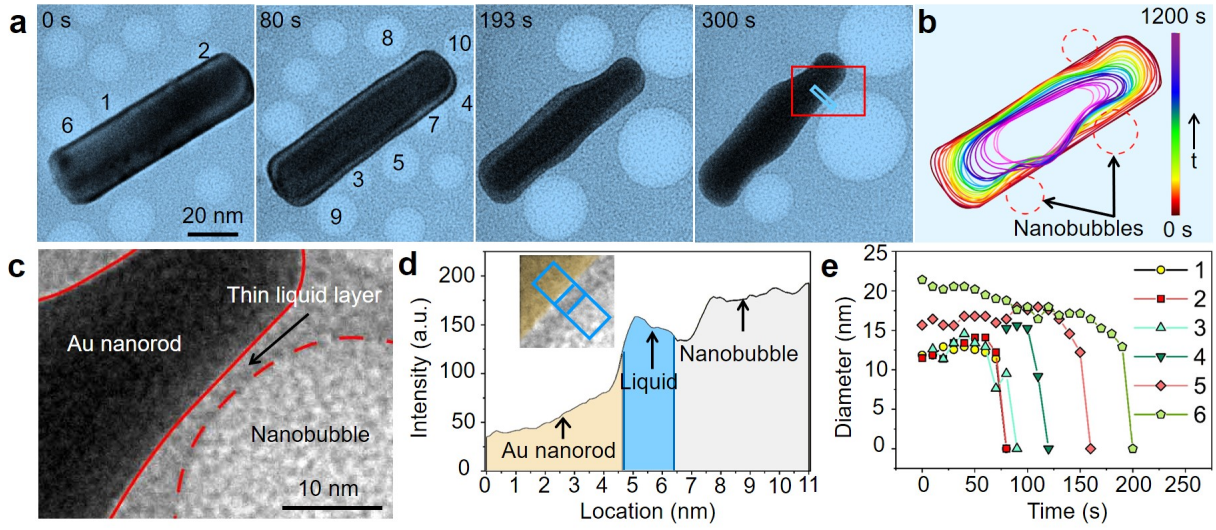

Fig. 2. Real-time-observation of etching process of nanorod in the presence of O_2 gas nanobubbles in a liquid cell. a, Time sequential TEM micrographs show the real-time shape evolution of the nanorod during the etching. Images are extracted from Video 1. **b**, The corresponding contour map highlights the indents are developed near the nanobubbles. **c**, The enlarged figure (marked with red rectangle in **a**) clearly shows the thin liquid layer between the nanorod and nanobubble. **d**, Intensity profile of the selected area shown in **a**. **e**, Diameter changes of nanobubbles with time. The numbers represent the different nanobubbles marked in **a**.

Figure 2 show the morphology evolution of a Au nanorod during etching with several nanobubbles surrounding the nanorod (also see Supplementary Video 2 for details). Sequential TEM images and the contour maps of the nanorod show that the nanorod develops indents near the nanobubbles as the etching proceeds (Fig. 2a,b). It is clear that materials at the indented areas are etched away instead of being redistributed to other parts of the nanorod (Supplementary Fig. 5). Etching of the Au nanorod in this scenario is drastically different from that without a gas nanobubble in the near distance, in which the Au nanorod shows a smooth surface with ellipsoidal shape during etching (Supplementary Fig. 4 and Supplementary Video 1) (*23*). It is noted that the

nanobubbles are not in direct contact with the Au nanorod while the indent is developed. A thin liquid layer between them can be identified, see an enlarge image in Fig. 2c and the intensity profile of the selected rectangle across the interfaces (in Fig. 2a) in Fig. 2d. This implies that the etching at the indented areas results from the solid-liquid-gas reactions, unlike the solid-liquid etching process in Supplementary Fig. 4.

We also note that most nanobubbles shrink and disappear eventually during etching of the Au nanorod, as shown in Fig. 2e. It suggests that nanobubbles participate in the reaction as a reactant not a reaction product from unexpected side reactions. The growth of certain nanobubble are attributed to Ostwald ripening between nanobubbles, which are highlighted separately in Supplementary Fig. 6. In addition to likely being consumed during the Au etching process, nanobubbles shrinking slowly may result from the instability of nanobubbles due to other factors, such as the increased local ion concentration (*37*).

In order to quantify the enhanced etching of the Au nanorod by nanobubbles, we select a Au nanorod with a nanobubble near one tip. Sequential images show the Au nanorod is etched away while the distance of the nanobubble to the tip varies (0-5 nm; see Fig. 3a and Supplementary Video 3). The contour map highlights that etching along the long axis is fast, while no obvious change in the diameter (Fig. 3b). Significantly higher longitudinal etching rates V_L are observed when the distance of nanobubble is about 1 nm or less. V_L is drastically reduced and maintains a constant when the distance of nanobubble is larger than 1 nm (Fig. 3c). Measurement results of additional nanorods agree with this observed trend (Supplementary Figs. 7-10). We further trace the length changes of nanorod with time and the corresponding changes of the distance between the nanobubble and the tip (d) are also plotted (Fig. 3d). The etching rate (V_L) can be estimated by

the slopes of linear fitting. Based on the values of V_L, three stages can be identified (stage I: 0.043 nm/s, stage II: 0.31 nm/s and stage III: 0.056 nm/s).

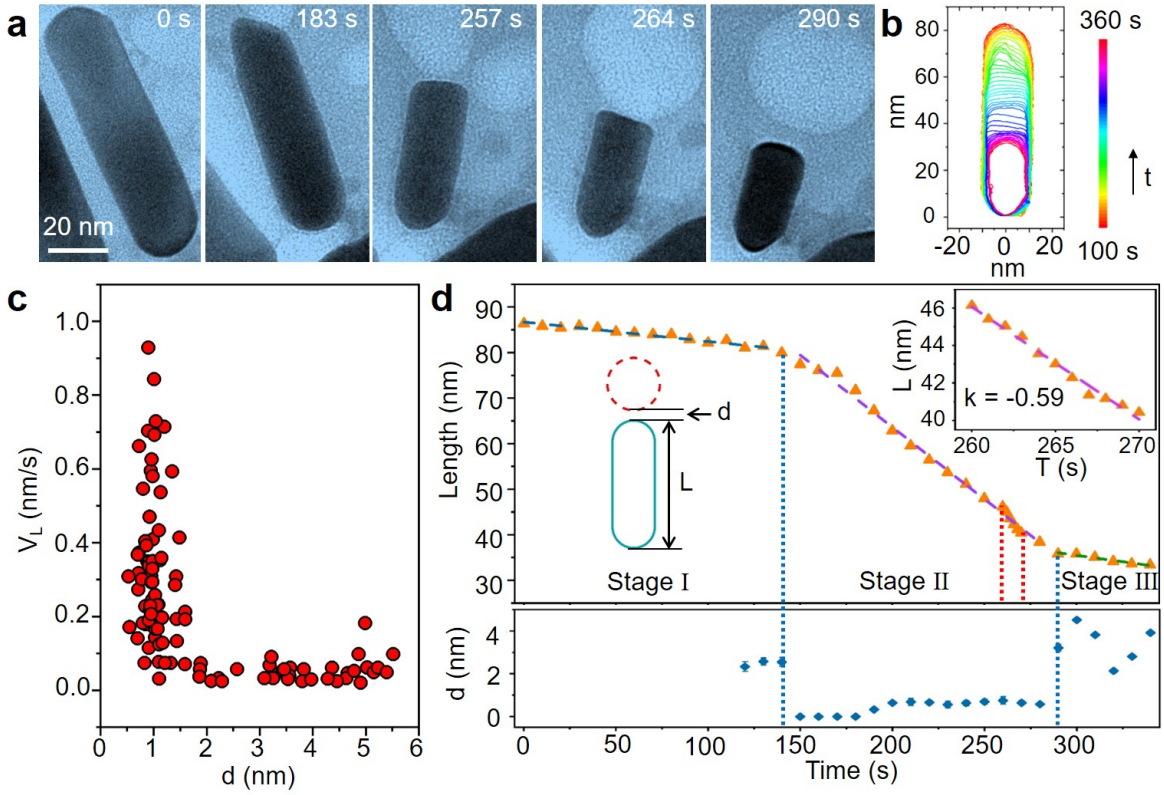

Fig. 3. Real-time observation of a gold nanorod etching with a O_2 gas nanobubble at an end of nanorod. a, Sequential TEM images of the Au nanorod during etching. b, The time-labeled contours show the shape evolution of the gold nanorod in **a**. **c**, A statistic plot showing the longitudinal etching rate as a function of the distance between the nanobubble and nanorod surface. **d,** Length changes of the gold nanorod as a function of time. Corresponding distance between nanorod and nanobubble is plot below. The inset is a magnified view of the plot during 260-270 s

with an average etching rate of 0.59 nm/s, which is an order of magnitude faster than that in stage I. Especially at the 266 s, the etching rate reaches 0.9 nm/s, which is 20 times higher than stage I.

In stage I, there is no effective nanobubble close to the nanorod. It shows a low etching rate (0.043 nm/s). As the nanobubble gradually approaches the nanorod close to 1 nm (starting at 150 s), the etching rate increases significantly with an average of 0.31 nm/s (stage II). Especially after two adjacent nanobubbles are merged, the average etching rate and highest etching rate are 0.59 nm/s and 0.9 nm/s, which are ten-fold and twenty-fold higher than that in stage I, respectively (see the inset in Fig. 3d during 260 s to 270 s and Supplementary Fig. 11). We note that d is in the similar range during 260 s to 270 s. It suggests that the more reactant of gas molecules helps to enhance the etching. In stage III, the nanorod experiences slow etching again when the nanobubble moves far away (after 290 s; also see Supplementary Fig. 11). It is interesting that the accelerated etching disappears immediately as the nanobubble leaves the nanorod surface (Fig. 3a,d, Supplementary Figs. 12,13 and Supplementary Videos 3,4), which is consistent with the above rapid enhanced reaction when the nanobubble approaches 1 nm. It illustrates that the ultra-thin liquid layer between the solid and the liquid is the key to accelerating the reaction, rather than requiring gas to directly contact the solid surface. Furthermore, we also compare the ratios of longitudinal and transverse etching rate (V_L/V_D) of different nanorods with and without nanobubbles. The results also agree with the enhanced etching by nanobubbles (Supplementary Fig. 14).

To uncover the mechanisms of the accelerated etching by nanobubbles, we establish a simple model of the adsorbing process of O_2 molecules. The typical snapshots of O_2 molecules of a nanobubble adsorbing on the gold nanorod surface in an aqueous NaBr solution by molecular dynamics (MD) simulations are illustrated in Fig. 4a (I) and (II). The distance between the

nanobubble and the gold nanorod surface, d, varies from 0.8 nm to 6 nm. First, as shown in Fig. 4b, the adsorbing site of Br^- ions in its density distribution near the Au nanorod surface remains at δz=0.6 nm in the presence of oxygen, suggesting that the accelerated etching of Au does not arise from the local ion concentrations but the reaction between O_2 and nanorod. Second, we considered O_2 diffusion pathway in the liquid layer. The adsorbing rate of O_2 molecules, $V_A=1/<T_A>$, could be estimated by their average adsorbing time T_A on the gold nanorod surface. The adsorbing time T_A refers to diffusion time of the O_2 molecules adsorbed on the gold nanorod surface in the MD simulations. As illustrated in Fig. 4c, a dependence of the adsorbing rate on the distance between the nanobubble and the gold nanorod surface is identified. A much higher value of V_A relates to the critical distance about 1.0 nm or less and it is drastically reduced when the distance is larger than 1 nm. The calculated adsorbing rates are thus in good agreement with the observed experimental results of the etching rates in Fig. 3c. The high absorbing rate within 1.0 nm indicates the existence of strong attractive forces from the Au nanorod surface within a close range. The low absorbing rate suggests the process is governed by the slow diffusion of O_2 molecules when they are far away (>1.0 nm).

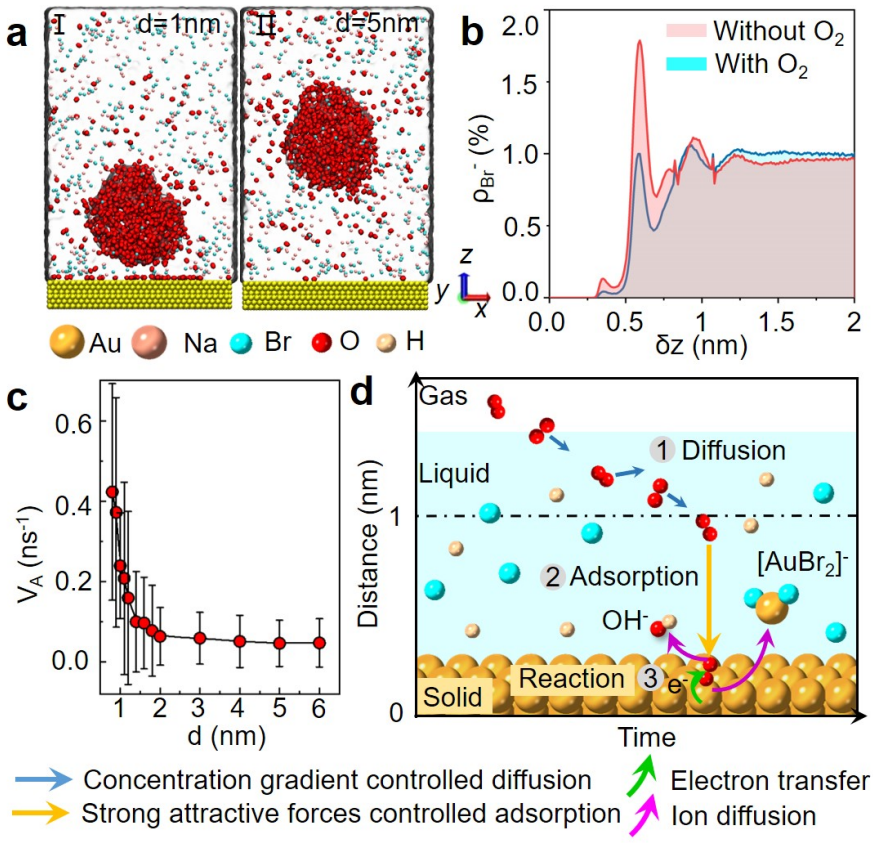

Fig. 4. The O_2 gas involved Au nanorod etching pathway. a, Schematic of MD calculation model of O_2 molecules of a nanobubble, with a distance d=1 nm (I) and 5 nm (II) from the Au nanorod surface, adsorbing on the gold nanorod surface at time t= 2 ns. **b**, Distributions of Br^- ions as a function of the distance to the gold nanorod surface with and without O_2 molecules. **c**, The adsorption rate of O_2 Molecules, V_A, as a function of the distance between the nanobubble and Au nanorod surface **c**. **d**, Schematic illustration of the Au nanorod etching pathway in the presence of O_2, including (1) the O_2 diffusion controlled by concentration gradient, (2) the adsorption of O_2 molecules by the strong attractive van der Waals interactions with Au atoms and (3) reaction on the nanorod surface.

Combining nanorods and nanobubbles tracking with MD simulations, we expect two different O_2 transfer mechanisms participating in the solid-liquid-gas reactions. When the distance

between O_2 molecules and nanorod surface is larger than a critical distance (~1 nm), the slow O_2 molecules diffusion is expected. When the distance is reduced to less than the critical distance, the O_2 molecules are easily adsorbed on the Au nanorod surface by the strong attractive van der Waals interactions and the faster etching is expected. The corresponding solid-liquid-gas etching pathway with different distances between nanorod and nanobubble is summarized in Fig. 4d. Identification of the mechanisms of accelerated solid-liquid-gas reactions opens the future opportunity to design and control complex reactions that involve triple phases. We also propose several promising strategies for accelerating the triple-phase reaction through specific ventilation approaches in different scenarios (Supplementary Fig. 15).

In summary, we captured the solid-liquid-gas etching process of Au nanorod in real-time at nanoscale using liquid cell TEM. It identifies two distinct reaction scenarios dependent on the liquid layer thickness which determines the gas transport mechanism. When the liquid layer thickness reduces into strong short-range attractive forces range, oxygen molecules in the bubbles can directly adsorb on Au nanorods surface and lead to a faster reaction rate. This study enhances our knowledge of reaction pathway on triple-phase boundary and provides a promising approach to modify solid-liquid-gas reaction rate. Moreover, it shows that liquid cell TEM provides for observation and mechanistic understanding of solid-liquid-gas reaction at the relevant time and length scales, which offers great potential for addressing many fundamental issues where nanoscale gas and liquid states involved.

References and Notes:

1. Snyder, J., Fujita, T., Chen, M., & Erlebacher, W. J. Oxygen reduction in nanoporous metal–ionic liquid composite electrocatalysts. *Nat. Mater.* **9**, 904-907 (2010).

2. Irvine, J. T. S. et al. Evolution of the electrochemical interface in high-temperature fuel cells and electrolysers. *Nat. Energy*. **1**, 15014 (2016).

3. Qiao, M. & Titirici, M-M. Engineering the Interface of Carbon Electrocatalysts at the Triple Point for Enhanced Oxygen Reduction Reaction. *Chem. Eur. J.* **24**, 18374-18384 (2018).

4. Tang, C., Wang, H-F. & Zhang, Q. Multiscale Principles To Boost Reactivity in Gas-Involving Energy Electrocatalysis. *Acc. Chem. Res.* **51**, 881-889 (2018).

5. Pan, C., Guo, M., Han, W., Wang, Z. & Wang, C. Study of corrosion evolution of carbon steel exposed to an industrial atmosphere. *Corros. Eng. Sci. Technol.* **54**, 241-248 (2019).

6. Bu, F. R., Li, J. N. & Huang, H. L. Effects of electrolyte thickness, chloride ion concentration, and an external direct current electric field on corrosion behaviour of silver under a thin electrolyte layer. *Corros. Eng. Sci. Technol.* **54**, 143-153 (2018).

7. Zhu, Y. P., Guo, C., Zheng, Y. & Qiao, S-Z. Surface and Interface Engineering of Noble-Metal-Free Electrocatalysts for Efficient Energy Conversion Processes. *Acc. Chem. Res.* **50**, 915-923 (2017).

8. Li, J. et al. Breathing-Mimicking Electrocatalysis for Oxygen Evolution and Reduction. *Joule* **3**, 557-569 (2019).

9. Lu, Z. et al. Superaerophilic Carbon-Nanotube-Array Electrode for High-Performance Oxygen Reduction Reaction. *Adv. Mater.* **28**, 7155-7161 (2016).

10. She, Z. W. et al. Combining theory and experiment in electrocatalysis: Insights into materials design. *Science* **355**, eaad4998 (2017).

11. Liu, M., Zhao, Z., Duan, X. & Huang, Y. Nanoscale Structure Design for High-Performance Pt-Based ORR Catalysts. *Adv. Mater.* **31**, 1802234 (2019).

12. Qiao, M. et al. Oxygenophilic ionic liquids promote the oxygen reduction reaction in Pt-free carbon electrocatalysts. *Mater. Horiz.* **4**, 895-899 (2017).

13. Lu, Q. et al. Highly porous non-precious bimetallic electrocatalysts for efficient hydrogen evolution. *Nat. Commun.* **6**, 6567 (2015).

14. Li, J., Johnson, G., Zhang, S & Su, D. In Situ Transmission Electron Microscopy for Energy Applications. *Joule* **3**, 4-8 (2019).

15. Zhu, R. C. When Catlysts Breathe. *Joule* **3**, 1–5 (2019).

16. Li, J. et al. Efficient electrocatalytic CO2 reduction on a three-phase interface. *Nat. Catal.* **1**, 592-600 (2018).

17. Kim, O. H. et al. Ordered macroporous platinum electrode and enhanced mass transfer in fuel cells using inverse opal structure. *Nat. Commun.* **4**, 2473 (2013).

18. Liu, Z., Sheng, X., Wang, D. & Feng, X. Efficient Hydrogen Peroxide Generation Utilizing Photocatalytic Oxygen Reduction at a Triphase Interface. *iScience* **17**, 67-73 (2019).

19. Sun, J. et al. Liquid-like pseudoelasticity of sub-10-nm crystalline silver particles. *Nat. Mater*. **13**, 1007–1012 (2014).

20. Zhou, Y. et al. In situ observation of atomic-scale stability limit of Cu nanoparticles. *Mater. Today Nano* **4**, 32–37 (2018).

21. Xu, H. et al. Dynamic structure-properties characterization and manipulation in advanced nanodevices. *Mater. Today Nano* **4**, 32–37 (2018).

22. Yang, J. et al. Formation of two-dimensional transition metal oxide nanosheets with nanoparticles as intermediates. *Nat. Mater.* **18**, 970–976 (2019).

23. Zheng, H. et al. Observation of Single Colloidal Platinum Nanocrystal Growth Trajectories. *Science* **324**, 1309-1312 (2009).

24. Ye, X. et al. Single-particle mapping of nonequilibrium nanocrystal transformations. *Science* **354,** 874-877 (2016).

25. Ou, Z., Wang, Z., Luo, B., Luijten, E. & Chen, Q. Kinetic pathways of crystallization at the nanoscale. *Nat. Mater.* **19**, 450–455 (2020).

26. Lou, L. et al. Atomic origins of water-vapour-promoted alloy oxidation. *Nat. Mater.* **17**, 514-518 (2018).

27. Zhu, C. et al. In-situ liquid cell transmission electron microscopy investigation on oriented attachment of gold nanoparticles. *Nat. Commun.* **9**, 421 (2018).

28. Smeets, P., Cho, K., Kempen, R., Sommerdijk, N. & Yoreo, J. Calcium carbonate nucleation driven by ion binding in a biomimetic matrix revealed by in situ electron microscopy. *Nat, Mater.*, **14**, 394-399 (2015).

29. Xu,T. & Sun, L. Investigation on material behavior in liquid by in situ TEM. *Superlattices Microstruct.* **99**, 24-34 (2016).

30. Hutchings, G. J. *Heterogeneous Gold Catalysis. ACS Cent. Sci.* **4**, 1095-1101 (2018).

31. Fujita, T. et al. Atomic origins of the high catalytic activity of nanoporous gold. *Nat. Mater.* **11**, 775-780 (2012).

32. Pflästerer, D. & Hashmi, A. S. Gold catalysis in total synthesis–recent achievements. *Chem. Soc. Rev.* **45**, 1331-1367 (2016).

33. Jiang, Y. et al. In situ Study of Oxidative Etching of Palladium Nanocrystals by Liquid Cell Electron Microscopy. *Nano Lett.* **14**, 3761-3765 (2014).

34. Woehl, T. J. & Abellan, P. Defining the radiation chemistry during liquid cell electron microscopy to enable visualization of nanomaterial growth and degradation dynamics. *J. Microsc.* **265**, 135-147 (2017).

35. Schneider, N. M. et al. Electron−Water Interactions and Implications for Liquid Cell Electron Microscopy. *J. Phys. Chem. C* **118**, 22373-22382 (2014).

36. Hauwiller, M. R. et al. Gold Nanocrystal Etching as a Means of Probing the Dynamic Chemical Environment in Graphene Liquid Cell Electron Microscopy. *J. Am. Chem. Soc.* **141,** 4428-4437 (2019).

37. Nirmalkar, N., Pacek, A. W., & Barigou, M. Interpreting the interfacial and colloidal stability of bulk nanobubbles. *Soft Matter* 14, 9643-9656 (2018).

Methods

Gold nanorods. Gold nanorods (Au NRs) were synthesized according to a seed-mediated method developed by Ye et al(*38*). The TEM image and Energy dispersive spectra (EDS) elemental

mapping of original Au NRs are shown in Supplementary Fig. 1. The concertation of Au nanorods aqueous solution used in the experiment is 50 μg/ml.

Ex-situ experiment. To demonstrate the ability of O_2 to oxidize Au NRs, 0.5 ml Au NRs solution was mixed with 0.5 ml of 1 M HBr and then maintained at 70 ℃ with continuous bubbling of air. The control experiment was carried out under the same condition but without additional air supply. The color of the solution with bubbling air turns into colorless soon within 5 min which also suggests that O_2 can oxidize Au NRs into colorless $AuBr_2^-$ (*39*). However, the color of the solution without bubbling air only shows a slightly lighter after 20 min. Ex-situ characterization of nanorods are carried out using Titan 80-300 and ThemIS with imaging corrector operated at 300 kV.

In situ TEM experiment. The in-situ experiments were carried out using FEI Tecnai G20 operated at 200 kV. An incident electron dose rate of 200 $e^-/Å^2 \cdot s$ to 800 $e^-/Å^2 \cdot s$ is maintained for the study. We used Digital Micrograph to measure the images.

Electron energy loss spectroscopy (EELS). The EELS was carried out on Tecnai F20 equipped with a monochromator operated at 200 kV. The sample was made in the same method with the in-situ experiment except that the solution used here is pure water without HBr. EELS spectrum of O_2 was obtained under the TEM mode from the area that is constantly bubbling after being illuminated with an extended period of time (Fig. 1b, Supplementary Fig. 3). The EELS spectrum of water was collected immediately under the electron beam illumination and no nanobubble was generated during the acquisition time. The EELS spectra from water without nanobubbles shows an obvious peak at ~ 532 eV, which consistent with O K-edge recorded from pure water (*40,41*). However, the EELS spectra from bubbling water not only shows a peak at ~532 eV, but also a peak at ~527 eV. The EELS spectra (Gatan EELS Atlas) from air containing a mixture of molecular

oxygen and molecular nitrogen shows the O K-edge at ~527 eV. Thus, the peak at ~527 eV recorded from bubbling water is the evidence for production of molecular O_2.

Computational Models and Methods. In our MD simulations, the aqueous solution layer is ~10.0×10.0×16 nm^3 with 1052 gas molecules (O_2) and the typical concentration of NaBr is 0.44 mol/L (about 20% maximum saturation with 35160 water molecules and 293 NaBr). Atoms on the (100) facet of the Au nanorod (face centered cubic (fcc) structure) are set to be fixed. The extended simple point charge (SPC/E) water model is used, and the long-range electrostatic interaction is treated with the particle-mesh Ewald method with a real space cutoff of 1.2 nm. The cutoff distance of the van der Waals interaction is also set to be 1.2 nm. The simulation is performed in the canonical (NVT) ensemble at 300 K for 10 ns and 10 ensemble simulations from different initial conditions are considered. The adsorbing time and adsorbing rate are calculated by the relative ensemble averages *(42,43)*.

Electron dose and radiolysis products estimation. We first simply estimate the irradiation dose absorbed by water. The electron dose rate and steady state concentration of radiolytic chemical species are calculated according to previous reports (*44*). Gray per second (Gy/s) which is defined as the adsorption of one joule of energy per kilogram per second of water is used as the unit for dose rate to describe the radiation effect of incident electrons upon the thin liquid film.

$$\Phi = \frac{10^5 SI}{\pi a^2}(\mathrm{Gy/s}) \qquad \text{S1}$$

Here S (MeV electron cm^2/g) represents the stopping power in water, I (C/s) is the electron beam current and a (m) is the beam radius. The factor of 10^5 (m^2 electron Gy g/cm^2 MeV C) converts the units to Gy/s. Electron stopping power of water is adopted from the ESTAR database available from NIST (*45*). Hence, the dose rates in the in-situ experiment with nanobubbles are 1.7×10^9

(Gy/s) and 9.2×10^8 (Gy/s). The corresponding steady state concentration of H_2 and O_2 can be approximated with a power law

$$C_{ss,i}\sim\alpha_i\Phi^{\beta_i} \quad \text{S2}$$

Species	Steady State Concentration (mM) at dose rate of 1.7×10^9 (Gy/s)	Steady State Concentration (mM) at dose rate of 9.2×10^8 (Gy/s)
Hydrogen (H_2)	3.7	2.7
Oxygen (O_2)	0.32	0.21

Table 1: Steady state concentration of radiolytic species in the liquid cell. Steady state concentration power law parameters α_i and β_i are obtained from the reference(*38*).

According to the previous calculation, the temperature changes of water caused by beam irradiation are only a few °C and the gases are more likely formed by the electrolysis of water molecules(*44*). The calculation shows that the amount of H_2 is about an order of magnitude higher than that of O_2. The concentrations of saturated H_2 and O_2 in the water are 0.8 mM (1 atm, 20 ℃) and 1.4 mM (1 atm, 20 ℃), respectively. Therefore, the oxygen nanobubbles are more difficult to form and the majority of nanobubble should be hydrogen bubbles, especially in the HBr solution. This is consistent with our experiment. We found that only less than 10% of the nanobubbles can accelerate the local etching, even though the nanobubbles were very close to the nanorods.

Data availability. The data that support the findings of this study are available from the corresponding authors upon request.

Code availability. Computer codes for the theoretical calculations in this work are available from the corresponding authors upon request.

Reference

38. Ye, X., Zheng, C., Chen, J., Gao, Y. & Murray, C. B. Using binary surfactant mixtures to simultaneously improve the dimensional tunability and monodispersity in the seeded growth of gold nanorods. *Nano Lett.* **13**, 765-771 (2013).
39. Tsung, C-K. et al. Selective Shortening of Single-Crystalline Gold Nanorods by Mild Oxidation. *J. Am. Chem. Soc.* **128**, 5352-5353 (2006).
40. Jungjohann, K. L., Evans, J. E., Aguiar, J. A., Arslan, I. & Browning, N. D. Atomic-Scale Imaging and Spectroscopy for In Situ Liquid Scanning Transmission Electron Microscopy. *Microsc. Microanal.* **18**, 621-627 (2012).
41. Aronova, M. A., Sousa, A. A. & Leapman, R.D. EELS characterization of radiolytic products in frozen samples. *Micron* **42**, 252-256 (2011).
42. Aqvist, J. Ion-Water Interaction Potentials Derived from Free Energy Perturbation Simulations. *J. Phys. Chem.* 94, 8021-8024 (1990).
43. Fang, G. & Chen, J. Hindered Gas Transport through an Aqueous Salt Solution Interface. *The Journal of Physical Chemistry C*, 122, 20774-20780 (2018).
44. Schneider, N. M. et al. Electron−Water Interactions and Implications for Liquid Cell Electron Microscopy. *J. Phys. Chem. C* **118**, 22373-22382 (2014).
45. NIST Stopping-Power and Range Tables: Electrons, Protons, Helium Ions. https://physics.nist.gov/PhysRefData/Star/Text/ESTAR.html

Acknowledgments: We gratefully acknowledge H. Zhang and H.-T. Zhang (SEU-FEI Nano-Pico Center, Southeast University) for support and useful discussions. **Funding:** The work at Lawrence Berkeley National Lab was supported by U.S. Department of Energy, Office of Science, Office of Basic Energy Sciences, Materials Sciences and Engineering Division under Contract No. DE-

AC02-05-CH11231 within the in-situ TEM program (KC22ZH). The work at Southeast University was supported by the National Natural Science Foundation of China (Grant Nos.: 51420105003, 11327901, 61601116, 61974021) and the National Science Fund for Distinguished Young Scholars (Grant No.: 11525415). J. C. acknowledges support of Natural Science Foundation of Shanghai (Grant No. 19ZR1463200) and Shanghai Supercomputer Center of China. W. W. acknowledges financial support from the China Scholarship Council (201806090114).

Author contributions: W.W., H.-P. F., H.-M.Z and L.-T.S. conceived and designed the experiments. W.W. and T.X. performed the experiments; J.-G. C., H.-S.M and H.-P.F developed the simulations. J.-Y.S.-G, H.D, and Q.B.Z took part in the discussion and data analysis; Z.-R.G and T.-T.B synthesized the samples; L.T.S. supervised the project and revised the paper with H.M.Z. and H.-P.F. The manuscript was written through contributions of all authors. All authors have given approval to the final version of the manuscript.

Competing interests: Authors declare no competing interests.

Supplementary Materials:

Supplementary Figures and Figure Captions 1 to 15

Supplementary Videos and Video Captions 1 to 4

Figures

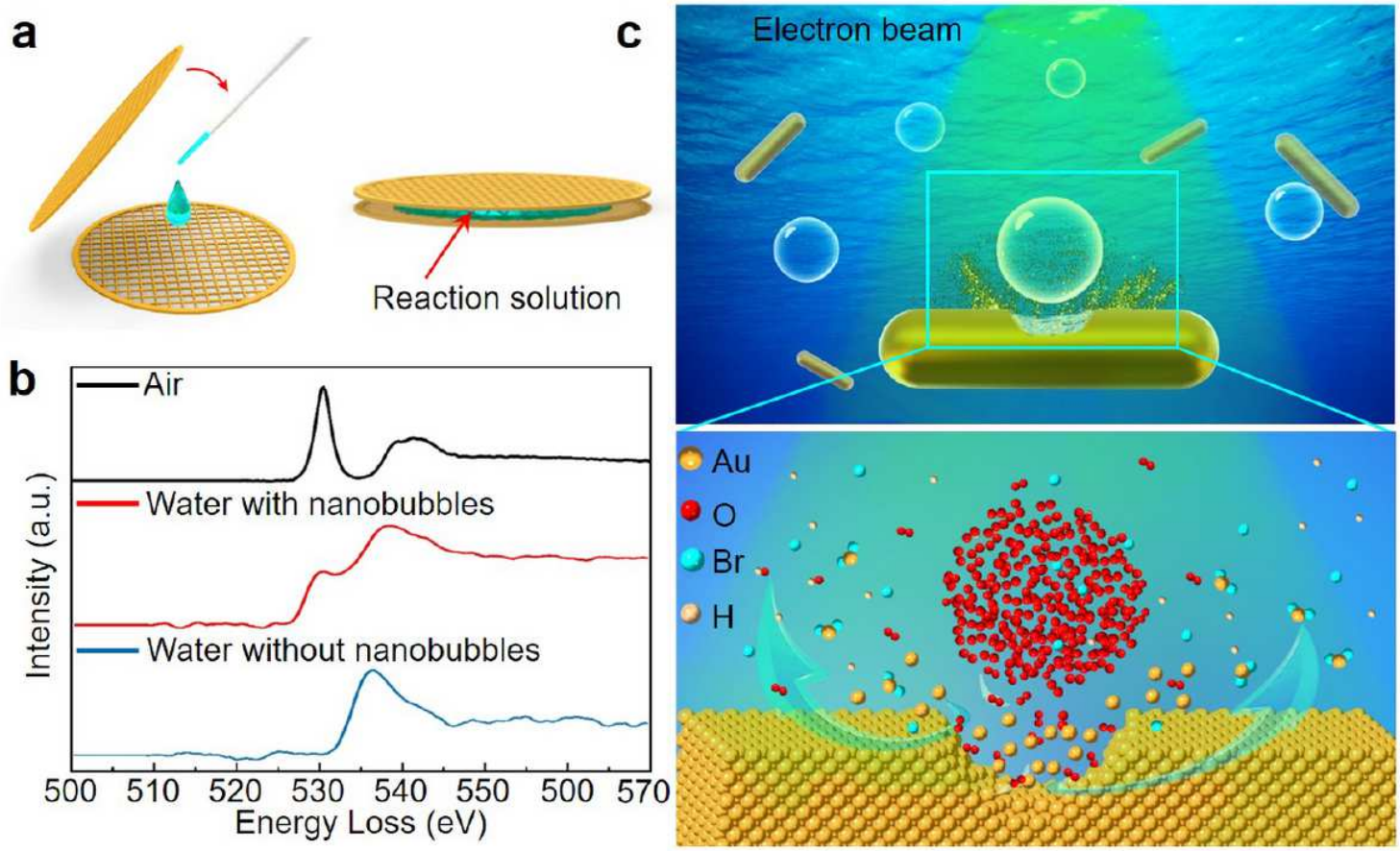

Figure 1

Schematic illumination of a solid-liquid-gas reaction established in a liquid cell. a, Schematic liquid cell encapsulating a reaction solution. b, Electron energy loss spectroscopy (EELS) show O K-edge of air (black, reference spectrum from Gatan EELS Atlas), water without nanobubble (blue) and the water with nanobubbles generated by electrolysis of water at a later stage (red). The O K-edge of water with nanobubbles shows evidence of molecular O2 at ~527 eV as compared with the reference spectrum from O2 gas (black). c, Schematic illustration of the etching of gold nanorods in HBr solution with O2 nanobubbles in the near distance.

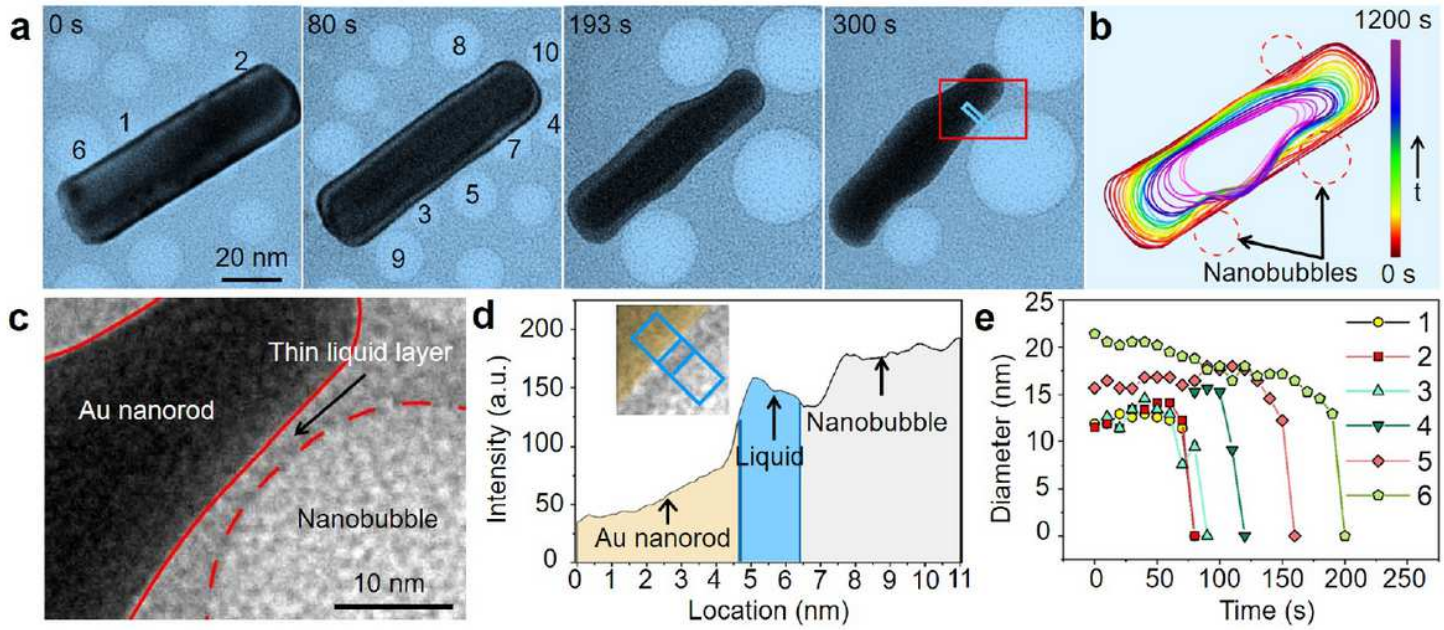

Figure 2

Real-time-observation of etching process of nanorod in the presence of O2 gas nanobubbles in a liquid cell. a, Time sequential TEM micrographs show the real-time shape evolution of the nanorod during the etching. Images are extracted from Video 1. b, The corresponding contour map highlights the indents are developed near the nanobubbles. c, The enlarged figure (marked with red rectangle in a) clearly shows the thin liquid layer between the nanorod and nanobubble. d, Intensity profile of the selected area shown in a. e, Diameter changes of nanobubbles with time. The numbers represent the different nanobubbles marked in a.

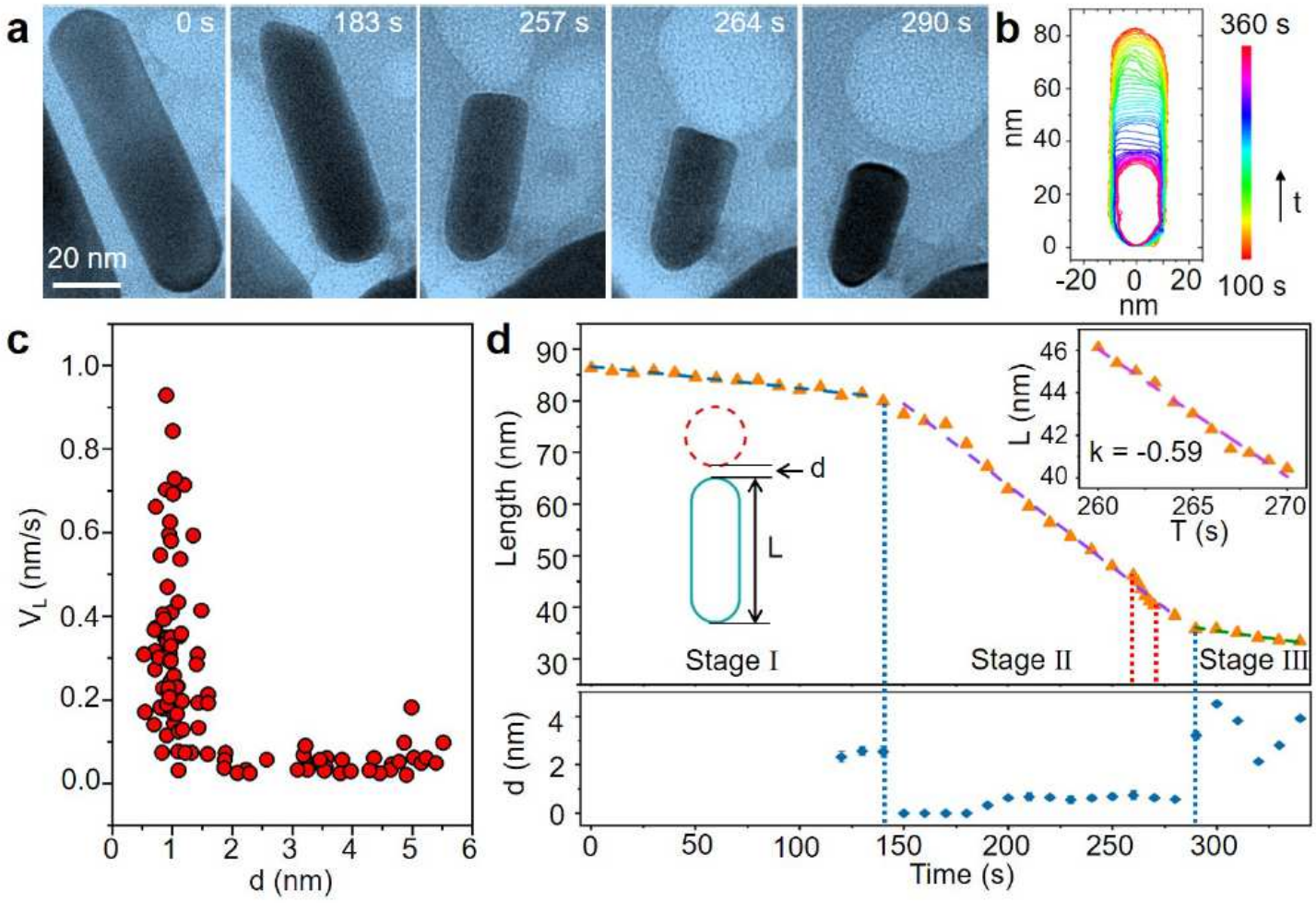

Figure 3

Real-time observation of a gold nanorod etching with a O2 gas nanobubble at an end of nanorod. a, Sequential TEM images of the Au nanorod during etching. b, The time-labeled contours show the shape evolution of the gold nanorod in a. c, A statistic plot showing the longitudinal etching rate as a function of the distance between the nanobubble and nanorod surface. d, Length changes of the gold nanorod as a function of time. Corresponding distance between nanorod and nanobubble is plot below. The inset is a magnified view of the plot during 260-270 s with an average etching rate of 0.59 nm/s, which is an order of magnitude faster than that in stage . Especially at the 266 s, the etching rate reaches 0.9 nm/s, which is 20 times higher than stage .

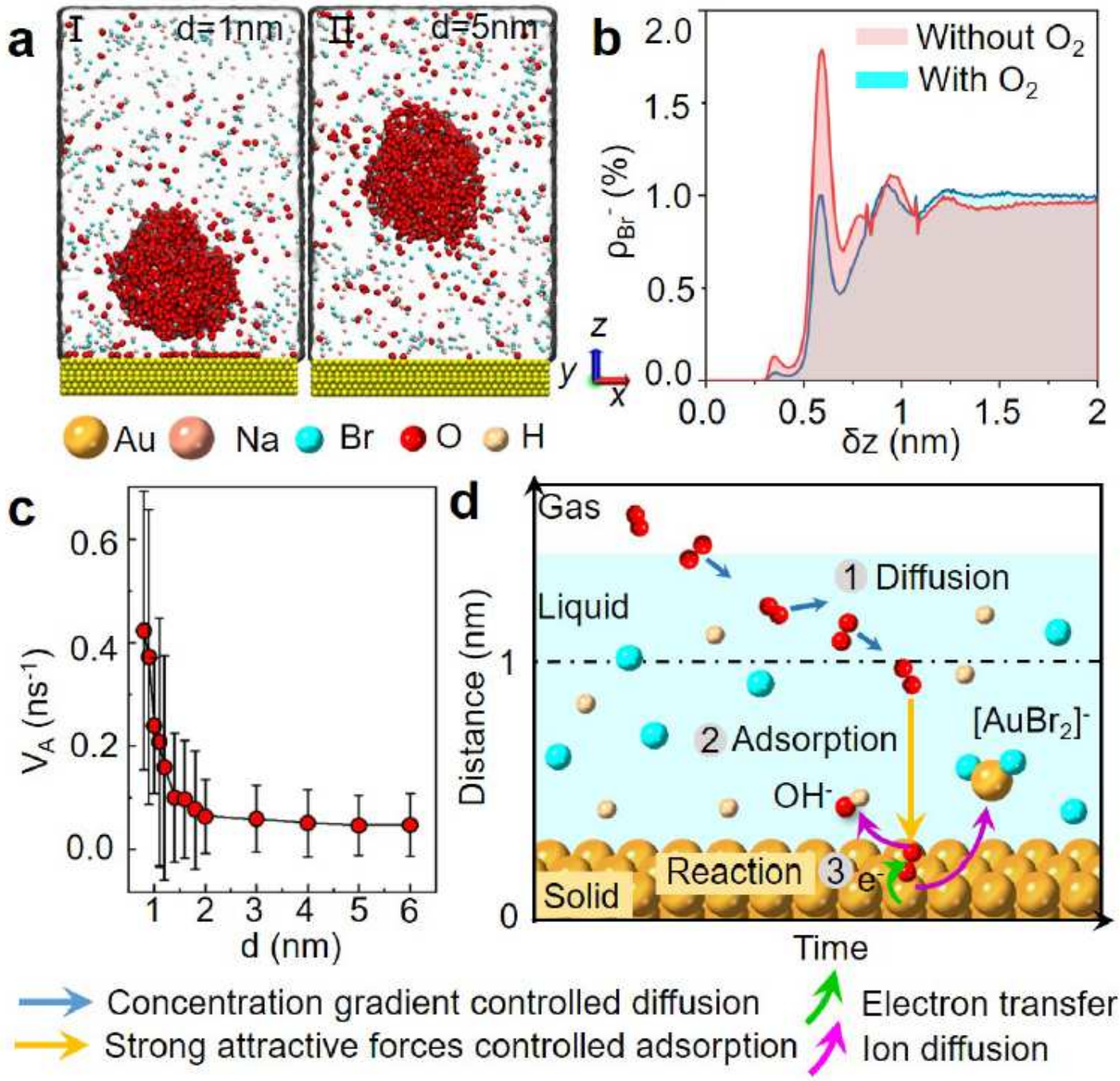

Figure 4

The O2 gas involved Au nanorod etching pathway. a, Schematic of MD calculation model of O2 molecules of a nanobubble, with a distance d=1 nm (I) and 5 nm (II) from the Au nanorod surface, adsorbing on the gold nanorod surface at time t= 2 ns. b, Distributions of Br- ions as a function of the distance to the gold nanorod surface with and without O2 molecules. c, The adsorption rate of O2 Molecules, VA, as a function of the distance between the nanobubble and Au nanorod surface c. d, Schematic illustration of the Au nanorod etching pathway in the presence of O2, including (1) the O2

diffusion controlled by concentration gradient, (2) the adsorption of O2 molecules by the strong attractive van der Waals interactions with Au atoms and (3) reaction on the nanorod surface.

Supplementary Files

This is a list of supplementary files associated with this preprint. Click to download.

- Video1.mp4
- Video2.mp4
- Video3.mp4
- Video4.mp4
- SupplementaryMaterials.pdf